# NbN films with high kinetic inductance for high-quality compact superconducting resonators

S. Frasca[1,2,3,*] I.N. Arabadzhiev,[1] S.Y. Bros de Puechredon,[1] F. Oppliger,[2,3] V. Jouanny,[2,3]
R. Musio,[1] M. Scigliuzzo,[2,3] F. Minganti,[2,3] P. Scarlino,[2,3] and E. Charbon[1]

[1]*Institute of Engineering, Swiss Federal Institute of Technology (EPFL), Neuchâtel 2002, Switzerland*

[2]*Institute of Physics, Swiss Federal Institute of Technology (EPFL), Lausanne 1015, Switzerland*

[3]*Center for Quantum Science and Engineering, Swiss Federal Institute of Technology (EPFL), Lausanne 1015, Switzerland*

Niobium nitride (NbN) is a particularly promising material for quantum technology applications, as it shows the degree of reproducibility necessary for large-scale superconducting circuits. We demonstrate that resonators based on NbN thin films present a one-photon internal quality factor above $10^5$ maintaining a high impedance (larger than $2\text{k}\Omega$), with a footprint of approximately $50 \times 100 \ \mu\text{m}^2$ and a Kerr nonlinearity of few tenths of a hertz. These quality factors, mostly limited by losses induced by the coupling to two-level systems, have been maintained for kinetic inductances ranging from tenths to hundreds of pico-Henry per square. We also demonstrate minimal variations in the performance of the resonators during multiple cooldowns over more than nine months. Our work proves the versatility of niobium nitride high-kinetic-inductance resonators, opening perspectives towards the fabrication of compact, high-impedance, and high-quality multimode circuits, with sizable interactions.

## I. INTRODUCTION

The possibility of tuning the magnitude of the inductance in superconducting circuits is paramount to achieve the high degree of control and flexibility required for quantum technology [1]. Two platforms have been mostly used to achieve high values of inductance: arrays of Josephson junctions (JJs) [2–6] or high-kinetic-inductance disordered thin films [7,8]. JJ devices are characterized by very low dissipation rates, and for this reason they are routinely used in circuit quantum electrodynamics (cQED) [9,10]. Usually, JJ-based circuits still exhibit large nonlinearities. To dilute such nonlinearity suitably for applications such as quantum-limited parametric amplifiers, arrays of JJs sacrifice compactness and add fabrication overhead [11,12].

Kinetic inductance is a promising novel resource for quantum technology [12–15]. For instance, superconducting high-kinetic-inductance (high-$L_k$) thin films have been used for several cryogenic applications, ranging from detectors [14,16,17] to amplifiers [15,18] and tunable filters [19,20]. In dirty superconductor thin films, the inductance depends on the Cooper pairs' carrier density [7], and it can be tuned by controlling the chemical composition of the films during deposition. From a cQED perspective, the advantages of high $L_k$ are manifold. Thin films give designers the freedom to operate with low or high impedance: for instance, when designing coplanar waveguide elements, by adjusting transmission line widths and gaps, it is possible to obtain impedance ranging from a few tens of ohms up to several kilo-ohms.

The ability to achieve high-impedance resonators and waveguides also leads to a higher range of achievable capacitive coupling between different circuit elements [21], as this coupling strength is proportional to the square root of the impedance of the microwave system. In turn, this allows the exploration of several regimes of light-matter interaction, from the strong to more exotic ultra-strong couplings [22,23]. Given the compact nature of high-$L_k$ film resonators, thin films can reduce the dimensions of both readout and control apparatus, and facilitate the realization of many-mode quantum devices [24]. Key to the success of this technology within a quantum framework is attaining regimes of low internal losses, where long coherence times can be maintained.

Many disordered superconductors have shown high kinetic inductance, e.g., NbN [24,25], NbTiN [15,18,26], and TiN [27], or materials composed of microscopic effective Josephson arrays such as the emergent granular aluminum [28]. Several groups have manufactured weakly disordered thin films that present considerable quality factors [27,29]. Consequently, thin films with moderate $L_k$

*simone.frasca@epfl.ch

have proved useful for quantum computing tasks [30], in particular for optical communication [31], quantum key distribution [32], and quantum teleportation [33].

Large-scale quantum applications will, however, also require a wide range of $L_k$ tunability and high control and reproducibility of the superconducting building blocks. In this work, we demonstrate that we fully control the kinetic inductance of NbN films (from 30 to 170 pH/□), maintaining a very high resonator quality in excess of $10^5$ at low photon number, with a high and reliable degree of reproducibility. According to the power and temperature dependence of the internal quality factor and the temperature dependence of the resonator frequency, we attribute to the saturable two-level systems (TLS) the main limiting factor to a single-photon lifetime [34]. Furthermore, our devices show no significant film degradation (ageing) over the course of different cooldowns nine months apart.

## II. DEVICE DESIGN AND FABRICATION

We fabricate planar lumped $LC$ resonators by etching 13-nm-thick NbN film, with typical impedance $Z = \sqrt{L_r/C_r}$ of 2 kΩ, where $L_r$ and $C_r$ are the inductance and capacitance of the resonator, respectively. The resonators are designed with inductor widths of 250 and 500 nm. The inductance contribution of the high-kinetic-inductance film is at least an order of magnitude larger than the geometric contribution, i.e., $L_r = L_g + L_k \approx L_k$. Indeed, for a 500-nm microstrip, considering a 525-µm-thick silicon dielectric ($\epsilon = 11.9$) to the ground, the geometric inductance per unit length $\mathcal{L}_g$ is roughly $1.8 \times 10^{-12}$ H/µm. For the same geometry, considering a sheet kinetic inductance of 30 (170) pH/□, the kinetic inductance per unit length $\mathcal{L}_k$ is $60 \times 10^{-12}$ ($340 \times 10^{-12}$) H/µm, hence approximately 30 (180) times larger than the geometric inductance. This leads to a relative contribution of the kinetic inductance with respect to the total inductance of 96% (99.4%) for the studied devices.

The fabrication begins with a 2-min dip in a 40% HF bath to remove the native oxide and possible contamination from the surface of an intrinsic, high-resistivity ($\geq 10$ kΩ cm), ⟨100⟩-oriented 100-mm Si wafer. There follows an NbN film bias sputtering [35] at room temperature in a Kenosistec rf sputtering system. After subsequent deposition of Ti/Pt alignment markers by an optical liftoff process and dehydration step at 150°C for 5 min, 80-nm-thick CSAR positive electron-beam resist is spin-coated at 4000 rpm on the wafer, and baked at 150°C for 5 min. With an electron-beam lithography (Raith EBPG5000+ at 100 keV) step, the devices are patterned on the resist through development in amyl acetate for 1 min, followed by rinsing in a solution 9:1 methylisobutylketone:isopropyl alcohol. The pattern is then transferred to the NbN using $CF_4$/Ar mixture and reactive ion etching with a power of 15 W for 5 min. The resist is stripped by means of Microposit remover 1165 heated at 70°C. Finally, the wafer is coated with 1.5 µm AZ ECI 3007 positive photolithography resist for device protection and diced.

The advantages of bias sputtering [35], i.e., application of an rf bias voltage on the substrate, resides in ion bombardment during the film deposition, which causes a reduction of the superconducting critical temperature and grain size, permitting the deposition of a polycrystalline material. The polycrystallinity improves the superconductor homogeneity and eases the device realization. The film behaves as an amorphous material with respect to etching procedures, and simultaneously maintains the advantageous properties of crystalline superconductors. For example, the low electron-phonon interaction time is barely changed, with important repercussions, such as enhanced maximum count rate in superconducting single-photon detectors [35]. To optimize the film properties, we fine-tune the nitrogen:argon partial pressures in the chamber across several fabrication runs, with pressure and substrate bias chosen to give the least roughness in the films. These steps also improve the reproducibility and yield of the samples.

## III. EXPERIMENTAL SETUP

After the fabrication, we glue the chips on a copper support with poly(methyl methacrylate) and wire-bond it to a customized printed circuit board. The copper support is then mounted on the cold finger installed at the mixing chamber stage of a BlueFors LD250 dilution refrigerator at a base temperature of 10 mK; see Fig. 1(a).

In order to test multiple devices in a single cooldown and to increase the experimental throughput, the devices are connected in transmission configuration through cryogenically operating coaxial switches (Radiall, R573 series), sharing both input and output lines; see Fig. 1(a).

Each sample is composed by seven resonators, capacitively coupled to a common 50 Ω coplanar transmission line, as in Fig. 1(b). The output line is connected to two cryogenic insulators (Low Noise Factory, LNF-ISISC4-8A series) to attenuate thermal noise injection from the amplifier, and a cryogenic low-noise amplifier (Low Noise Factory, LNF-LNC4-8C series) operating at the 4 K stage of the cryostat. Input and output lines are then connected at room temperature to a Vector Network Analyzer (Rohde & Schwarz, ZNA26 series) to acquire the scattering parameters.

The notch (or hanger [36]) configuration of resonators has been chosen for a precise estimation of the internal quality factor of the devices—they self-calibrate with respect to the transmission baseline—and this allows frequency multiplexing [36]. Moreover, the microwave feedline can be probed in dc to estimate the resistance-temperature characteristic curve and the critical temperature $T_C$. The latter has been measured with a
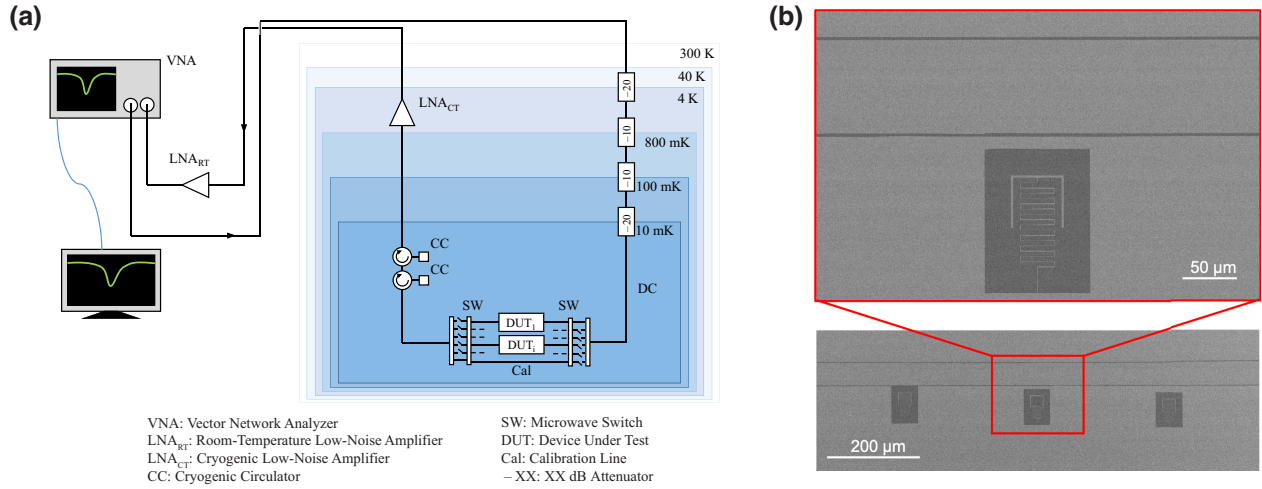
FIG. 1.    (a) Schematics for the cryogenic setup. The input lines are attenuated with 60-dB cryogenic attenuators distributed across the several stages of the cryostat as shown. (b) Scanning electron micrograph of a representative resonator. The hanger resonators are capacitively coupled to a 50 Ω microwave feedline, also realized in NbN. Each chip consists of two feedlines, each one coupled to seven frequency-multiplexed resonators, whose inductor width is either 250 nm or 500 nm.

closed-loop cryostat (PhotonSpot Inc.) with 800 mK base temperature.

## IV. RESULTS

### A. NbN film composition, critical temperature, and kinetic inductance

The kinetic inductance per square $L_k$ of the film can be expressed as [7]

$$L_k(T) = \frac{R_\square \hbar}{\pi \Delta} \frac{1}{\tanh[\Delta/(2k_B T)]}. \tag{1}$$

Here, $R_\square$ is the sheet resistance when the film is in the normal state, $T$ is the superconducting film temperature, and $\Delta$ is the superconducting band gap, which, according to Bardeen-Cooper-Schrieffer (BCS) theory, can be approximated to $\Delta \simeq 1.764 k_B T_C$ for $T \ll T_C$ with $T_C$ the critical temperature.

Figure 2 reports $T_C$ and $L_k(T)$, both measured and estimated according to Eq. (1), as functions of the $N_2$ flow during the sputtering deposition. The deposition conditions, critical temperatures, sheet resistance, estimated kinetic inductance, and critical current density $j_c$ of the thin films are reported in Table I. Increasing the $N_2$ concentration in the films causes an increment of impurities embedded in the films during the sputtering process. At low $N_2$, we notice a rise in the critical temperature. While the resistivity also increases, the ratio between these two in Eq. (1) does not compensate, causing a small drop in $L_k$ in the proximity of the stoichiometric condition, which for this deposition setting is found approximately at 2.5

sccm $N_2$ flux. Larger $N_2$ concentration increases the film disorder, causing a rise of film resistivity and a drop of critical temperature, both boosting the kinetic inductance.
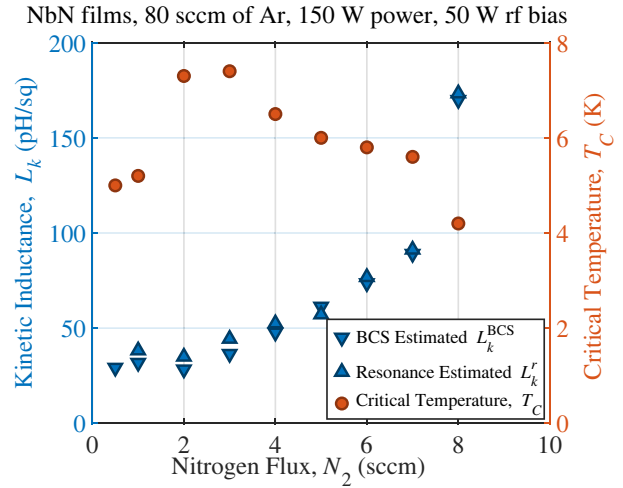


FIG. 2.    Critical temperature and estimated kinetic inductance for different NbN recipes. All the films presented are $13.0 \pm 0.6$ nm thick. With increasing $N_2$ flux, the films show first a sudden increase of $T_C$ corresponding to stoichiometric conditions, followed by a decrease caused by the large amount of impurities in the dirty superconductor. At the same time, the kinetic inductance first slightly drops due to the increase of $T_C$ as expected from Eq. (1), and then rapidly increases due to both $R_\square$ and $T_C$ contributions. The kinetic inductance was estimated both by BCS theory ($L_k^{BCS}$) and by fitting the resonant frequency of the resonators with Sonnet ($L_k^r$); see Appendix A.

TABLE I.   Measured and estimated main parameters of the deposited superconducting thin films. The kinetic inductivity of the films is estimated according to the procedure presented in Appendix A.

| Ar/N$_2$ (sccm) | $T_C$ (K) | $R_\square(T_{room})$ ($\Omega/\square$) | Resistivity, $\rho$ ($\mu\Omega$ cm) | RRR = $R(10\,\mathrm{K})/R(T_{room})$ | $L_{k,0}$ (pH/$\square$) | $j_c$ (A/cm$^2$) |
|---|---|---|---|---|---|---|
| 80/0.5 | 5.0 | 106 | 137.8 | $\cdots$ | 34.5 | $\cdots$ |
| 80/1 | 5.2 | 122 | 158.6 | 1.481 | 38.2 | $1.23 \times 10^6$ |
| 80/2 | 7.3 | 151 | 196.3 | 1.526 | 34.9 | $1.36 \times 10^6$ |
| 80/3 | 7.5 | 196 | 254.8 | 1.119 | 44.4 | $1.66 \times 10^6$ |
| 80/4 | 6.5 | 225 | 292.5 | 1.631 | 52.5 | $1.51 \times 10^6$ |
| 80/5 | 6.0 | 267 | 347.1 | 1.191 | 57.2 | $1.21 \times 10^6$ |
| 80/6 | 5.8 | 310 | 403.0 | 1.152 | 76.8 | $1.05 \times 10^6$ |
| 80/7 | 5.6 | 362 | 470.6 | 1.712 | 91.3 | $\cdots$ |
| 80/8 | 4.2 | 518 | 673.4 | 1.544 | 173.3 | $\cdots$ |

### B. Internal quality factor and Kerr nonlinearity

We model each cavity as a Kerr nonlinear resonator, described by the Hamiltonian

$$H = \hbar\omega_0 a^\dagger a + \hbar\frac{K}{2}(a^\dagger a)^2,$$

(2)

where $\hat{a}$ $(\hat{a}^\dagger)$ is the bosonic creation (annihilation) operator, $\omega_0$ is the resonant frequency of the cavity, and $K$ is the Kerr nonlinearity. These devices are also characterized by photon loss events, whose rate is given by $(\kappa + \gamma)$, with $\kappa$ the external coupling and $\gamma$ the internal losses. The resonator is driven at a frequency $\omega_d$ of intensity $P_{in}$.

For our devices, we measure the transmitted power $S_{21}$ of the resonator hanging to the feedline. To extract the parameters of a Kerr resonator in hanger configuration, we use input-output theory [37], and obtain

$$S_{21} = 1 - \frac{\kappa}{\kappa + \gamma}\frac{e^{i\phi}}{\cos\phi}\frac{1}{1 + 2i(\delta - \xi n)}.$$

(3)

Here the interdependent variables $\phi$, $\delta$, and $\xi$ depend on $K$, $\kappa$, $\gamma$, $\omega_0$, the drive frequency $\omega_d$, the photon number $n$, and other internal parameters of the resonator that can be independently measured, as detailed in Appendix C. As will be detailed later, the internal dissipation rate $\gamma$ has a nontrivial power dependence. Hence, we perform power scans of the devices to be able to estimate the total loss rate $(\kappa + \gamma)$ with respect to the average number of photons in the resonator $\langle n_{ph}\rangle$. We first estimate the resonator frequency $\omega_0$, as it corresponds to the dip in frequency of $S_{21}$ in the low-power regime. Then, to retrieve $\kappa$, $\gamma$, and $K$, we use a global fit routine at all powers, to increase the accuracy of the extrapolated values. In the linear regime at low power, we also benchmark our results for $\kappa$ and $\gamma$ using the Python package by Probst *et al.* [38], finding no significant discrepancies with respect to our routine.

In order to precisely estimate the internal quality factor and reduce fitting uncertainty, it is more convenient to approach a critical coupling condition $\kappa \approx \gamma$, where the

internal quality factor approximately matches the external coupling [36]. As the internal quality factor is not known *a priori*, we take full advantage of the notch configuration to engineer multiple couplings $\kappa$ for devices on the same chip. Fourteen hanger resonators are fabricated for each film, seven with an inductor width of 250 nm and seven with an inductor width of 500 nm. In Fig. 3 we present the measured and fitted transmitted power $S_{21}$ using Eq. (3) through the feedline for one of the critically coupled resonators as a function of the probe frequency and for several input powers.

Figure 4(a) reports the extracted quality factors of the 105 tested resonators in the linear regime (for Kerr-induced frequency shift much smaller than the resonator linewidth). The data points represent the averaged internal quality factor estimated for the seven resonators with different couplings $\kappa$ to the feedline; see Fig. 7(a) for the plot of the extracted $Q_i$ for all the measured resonators. The error bars represent the standard deviation between the internal quality factor of the different devices. We also include in the error bar the uncertainty deriving from the global fit of each resonator, although we notice that they are negligible with respect to the parameter spreading due to fabrication.

To quantify the self-Kerr nonlinearity $K$, we reach regimes of large photon numbers, where the effect of the nonlinearity is comparable to the resonator linewidth. In Fig. 4(b), we report the measured $K$ of the critically coupled tested resonators ($\kappa \approx \gamma$) for each film and width. The data for the resonators with 500-nm-wide (250 nm-wide) inductors are shown with triangles (circles). The self-Kerr nonlinearity increases with $L_k$, with a clear offset between the two inductor widths, as also reported in Ref. [25]. This is in agreement with the relation

$$K \propto \frac{L_{k,0}\omega_0^2}{(j_c wt)^{n_{fr}}},$$

(4)

obtained by replacing $I_c = j_c wt$ in the Kerr equation [see Appendix C, Eq. (C8)], where $j_c$ is the critical current density of the thin film, and $w$ and $t$, respectively, are the width
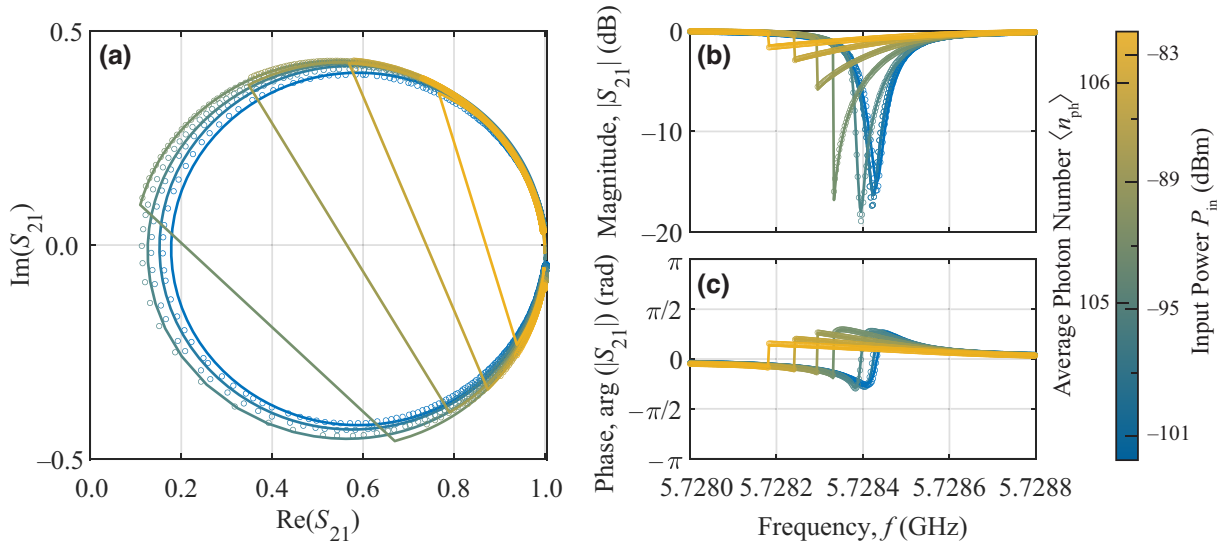
FIG. 3. Scattering parameter $S_{21}$ for a representative resonator. (a) Complex-plane representation of $S_{21}$ for seven different input powers. (b) Magnitude and (c) phase response as functions of the probe frequency of the same dataset presented in panel (a). Circles represent data points, while solid lines are the fitted functions according to Eq. (3).

and thickness of the inductor wire of the resonators. From this equation, we notice that the difference in width of the nanowire inductors clearly affects the value of $K$.

To highlight the dependencies of the self-Kerr nonlinearity $K$ on both kinetic inductance and inductor width, we plot $|K|/\omega_0^2$ in Fig. 7(b).

### C. Origin of the internal dissipation

All devices, except those with the highest $L_k$, show $Q_i$ around $10^5$ in the single-photon regime. For the devices

with the largest $L_k = 170$ pH/□, we argue that the nitrogen concentration of the film is approaching the limiting value of the superconductor–normal-metal transition (SNT), as observed for NbTiN in Ref. [39]. This argument is corroborated by the observation that the resonators with 250-nm-wide inductors did not exhibit any superconducting transition while reaching base temperature, while the $w = 500$ nm devices show a lower internal quality factor in the range of $10^4$ in the single-photon regime. These 170 pH/□ resonators, however, present $Q_i$ in excess of $10^5$ at a thousand-photon number, in line with the other films,
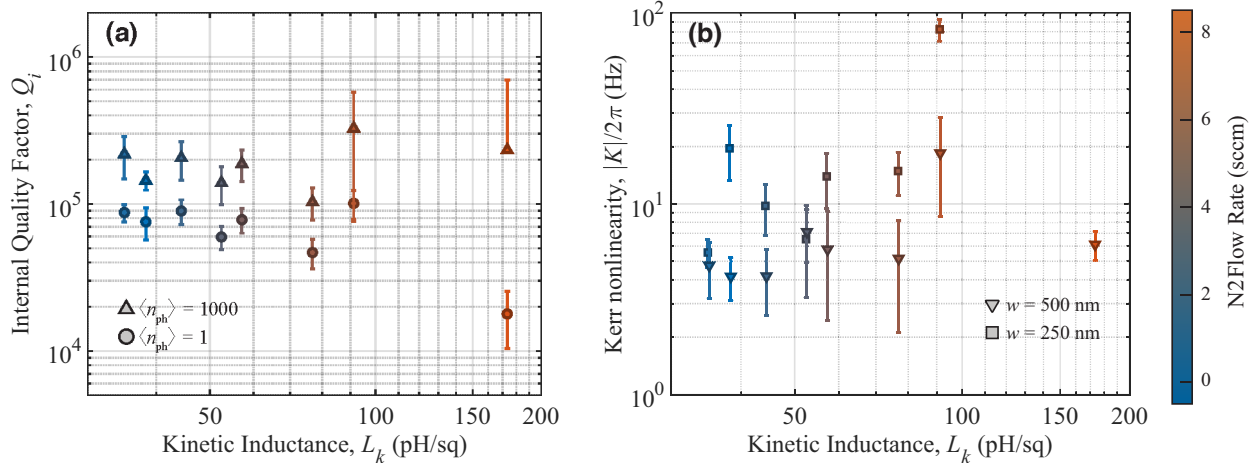


FIG. 4. (a) Dependence of the averaged resonator internal quality factor $Q_i$ with respect to kinetic inductance $L_k$. The extracted $Q_i$ at low photon number ($\langle n_{ph}\rangle \approx 1$) and high photon number ($\langle n_{ph}\rangle \approx 1000$) are represented with circle and triangle markers, respectively. (b) Extracted self-Kerr nonlinearity $K$ with respect to kinetic inductance $L_k$. The self-Kerr nonlinearity is extracted via global fit at different powers according to Appendix C. Triangles (squares) represent resonators with inductor width of 500 nm (250 nm). In both panels, error bars represent the distribution of the $Q_i$ and $K$ fitted according to Eq. (3) for the 14 devices (see also Fig. 7).

suggesting that the dissipation can be mainly attributed to a two-level system (TLS) hosted in highly disordered films [36,40]. While the TLS nature is still unclear, it is believed to be related to atoms tunneling between two sites of a disordered solid [41–43].

In order to describe the various mechanisms contributing to the internal quality factor as a function of input power, we write [24,34,44]

$$\frac{1}{Q_i} = \delta_0 + F\delta_{\mathrm{TLS}}^0 \frac{\tanh[\hbar\omega_0/(2k_BT)]}{(1 + \langle n_{\mathrm{ph}}\rangle/n_c)^\beta} + \frac{\alpha}{\pi}\sqrt{\frac{2\Delta}{hf_r}}\frac{n_{\mathrm{qp}}(T)}{n_s(0)\Delta}.$$
(5)

In this equation, $\delta_0$ is the residual loss rate of the resonator, i.e., the sum of the other loss contributions that are not described by the TLS nor the quasiparticle loss models.

The second contribution is due to TLS, which, according to the TLS model [43], generates a power- and temperature-dependent resonator loss. Here, $F$ is defined as the filling factor (the ratio between the electric field threading the TLS and the total electric field), $n_c$ is the characteristic photon number of TLS saturation, and $\delta_{\mathrm{TLS}}^0$ is the intrinsic TLS loss. While it is known that different interfaces (between metal, substrate, and air) host TLSs

[45,46], our measurements do not resolve these different loss channels, and we concentrate on a common TLS bath.

The third contribution is due to quasiparticles, where $\alpha$ is the ratio between kinetic and total inductance, $n_{\mathrm{qp}}(T) = n_s(0)\sqrt{2\pi k_BT\Delta}\,e^{-\Delta/k_BT}$ is the temperature-dependent population of quasiparticles [47], and $n_s(0)$ is the Cooper pairs' zero energy density of states. We assumed $\alpha$ to be 1, as the kinetic inductance contribution to the resonant frequency largely dominates the geometric inductance.

Figure 5 reports the measured quality factor for representative resonators of different films, close to critical coupling conditions, $\kappa \approx \gamma$, as a function of the photon number. We then fit the model in Eq. (5), and we find that the TLS contribution dominates the internal quality factor. We report the values of $F\delta_{\mathrm{TLS}}^0$ and $n_c$ obtained from the fits in Table II. Comparing them to what was previously found in Refs. [24,34], we find similar fitting values for the exponent $\beta$, close to 0.2 for all the tested devices. However, as reported in Fig. 5, the quality factors of the resonators start to improve after being populated with 50 photons on average (compare this number with the critical photon number $n_c$ reported in Table II). This value appears to be much larger than the one that can be inferred in similar NbN films from Ref. [24], which we attribute to a discrepancy in the
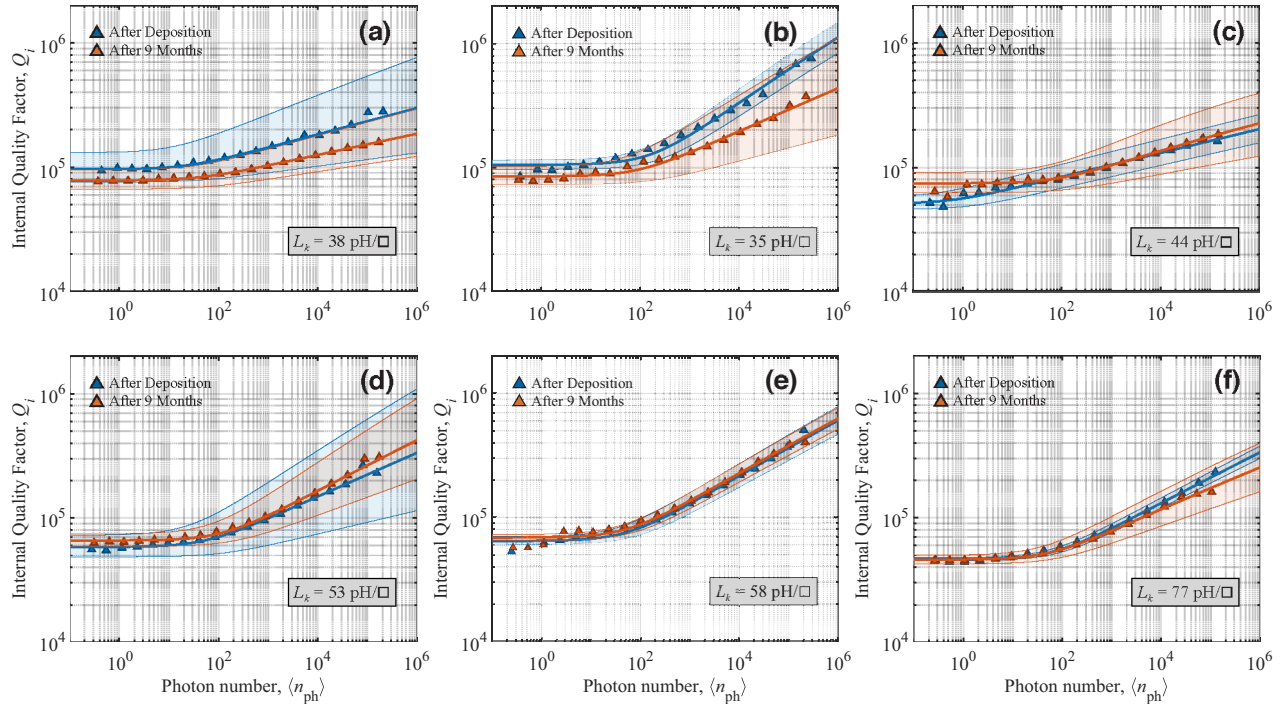


FIG. 5. Internal quality factors $Q_i$ as a function of photon number for NbN compact resonators realized on different films. Characteristic power-quality relations for devices made of films with increasing $N_2$ flow rate during deposition, namely from (a) 1 sccm to (f) 6 sccm. We performed power scans of critically coupled resonators of several film compositions to estimate the TLS fitting parameters according to Eq. (5). Blue (red) data points and fitting functions represent $Q_i$ measured right after (nine months after) film deposition. The results suggest a clear dominance of TLS as the main dissipation mechanism, as well as a more pronounced ageing effect for NbN films with lower $N_2$ concentration, in panels (a) and (b).

TABLE II. Main parameters of the superconducting devices for the films presented in Table I. For each film composition and resonator inductor width, the table reports only the values of the devices closest to critically coupled conditions ($\kappa \approx \gamma$).

| Device design | | Device properties | | | | | | |
|---|---|---|---|---|---|---|---|---|
| ID | Width (nm) | $\omega_0/2\pi$ (GHz) | $\kappa/2\pi$ (kHz) | $\gamma/2\pi$ (kHz) | $K/2\pi$ (Hz) | $F\delta_{\mathrm{TLS}}^0$ ($\times 10^{-5}$) | $n_c$ | $\Delta f_{\mathrm{age}}$ (MHz) |
| 801-500 | 500 | 5.58 | 86.95 | 57.52 | $-2.40$ | $1.02 \pm 0.16$ | $34.14 \pm 12.97$ | 3.42 |
| 801-250 | 250 | 4.95 | 112.87 | 68.00 | $-19.58$ | $1.40 \pm 0.05$ | $9.69 \pm 4.35$ | $\cdots$ |
| 802-500 | 500 | 5.87 | 74.51 | 61.77 | $-3.05$ | $1.00 \pm 0.03$ | $47.07 \pm 11.08$ | 3.78 |
| 802-250 | 250 | 5.17 | 40.59 | 66.21 | $-5.56$ | $1.22 \pm 0.27$ | $42.84 \pm 48.82$ | $\cdots$ |
| 803-500 | 500 | 5.95 | 91.88 | 95.96 | $-4.17$ | $1.83 \pm 0.12$ | $1.74 \pm 1.58$ | 4.83 |
| 803-250 | 250 | 5.15 | 50.42 | 66.66 | $-11.50$ | $1.31 \pm 0.07$ | $44.38 \pm 16.56$ | $\cdots$ |
| 804-500 | 500 | 5.49 | 123.21 | 95.31 | $-7.13$ | $1.69 \pm 0.20$ | $77.03 \pm 34.87$ | 4.00 |
| 804-250 | 250 | 4.74 | 45.52 | 90.26 | $-9.59$ | $1.88 \pm 0.094$ | $64.42 \pm 22.21$ | $\cdots$ |
| 805-500 | 500 | 5.72 | 105.78 | 91.09 | $-5.77$ | $1.53 \pm 0.15$ | $47.82 \pm 29.05$ | 3.76 |
| 805-250 | 250 | 5.06 | 59.69 | 73.91 | $-13.94$ | $1.41 \pm 0.07$ | $51.64 \pm 14.33$ | $\cdots$ |
| 806-500 | 500 | 4.93 | 76.049 | 111.30 | $-5.17$ | $2.16 \pm 0.17$ | $48.56 \pm 18.93$ | 3.28 |
| 806-250 | 250 | 4.37 | 64.83 | 132.39 | $-14.88$ | $2.84 \pm 0.19$ | $22.71 \pm 12.56$ | $\cdots$ |
| 807-500 | 500 | 6.47 | 64.81 | 42.17 | $-18.46$ | $0.67 \pm 0.05$ | $94.46 \pm 50.58$ | $\cdots$ |
| 807-250 | 250 | 6.59 | 49.06 | 62.92 | $-82.39$ | $1.43 \pm 0.63$ | $2.23 \pm 4.27$ | $\cdots$ |
| 808-500 | 500 | 3.34 | 45.63 | 233.55 | $-6.23$ | $6.72 \pm 0.29$ | $30.84 \pm 12.42$ | $\cdots$ |

photon-number expressions: see Eq. (C5), in comparison to Ref. [48].

To further show the dominance of TLS, we investigated the resonator's quality factor evolution at different operating temperatures. The cryostat was slowly warmed up from a base temperature of 15 mK to a temperature of almost 1 K in a controlled way, and the resonator spectrum was acquired at $\langle n_{\mathrm{ph}} \rangle \approx 50$. The evolution of the extracted internal quality factor $Q_i$ and resonator resonant frequency $\omega_0$ are reported in Fig. 6(a).

In addition, we characterize the TLS and quasiparticle contributions using the frequency shift of the resonators at different temperatures [see Fig. 6(b)]. Indeed, we have that [34]

$$\frac{\Delta f}{f_r} = \frac{F\delta_{\mathrm{TLS}}^0}{\pi}\left(\mathrm{Re}\left\{\Psi\left(\frac{1}{2} + \frac{hf_r}{2i\pi k_B T}\right)\right\} - \ln\frac{hf_r}{2\pi k_B T}\right) - \alpha\frac{\Delta L_k}{L_k}, \tag{6}$$

where $\Psi$ is the digamma function [44], $\Delta L_k/L_k$ is the kinetic inductance change, $L_k(T) = \mu_0\lambda^2(T)(l/wd)$, and $\lambda(T)$ is the temperature-dependent London penetration depth.
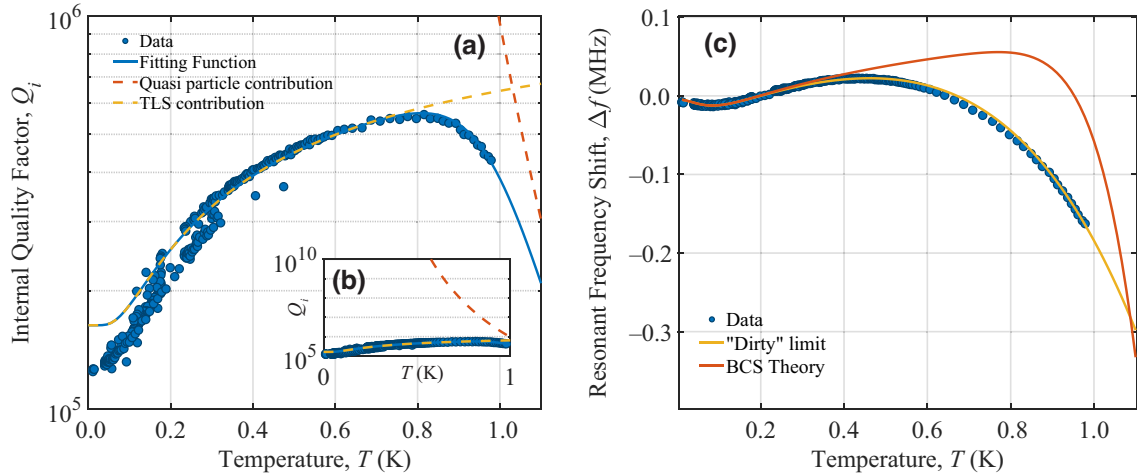


FIG. 6. (a) Temperature dependence of internal quality factor $Q_i$ for device 803-500 (see Table II). Inset (b) shows a wider view of panel (a) for $Q_i$ between $10^5$ and $10^{10}$, reported to highlight the expected evolution of the quasiparticle contribution to losses. Dashed red (yellow) lines represent the model of the contribution of quasiparticle (TLS) losses according to Eqs. (5) and (6), respectively. (c) Resonant frequency shift $\Delta f$ extracted from the same resonator as analyzed in panel (a). The validity of the quasiparticle and TLS parameters extracted from Eq. (5) is confirmed by agreement with the resonant frequency shift $\Delta f$ predicted by Eq. (6).

We assume that the film behaves as a superconductor in the dirty limit. As such, we have

$$\frac{\Delta L_k}{L_k} = \frac{\lambda^2(T) - \lambda^2(0)}{\lambda^2(0)} \propto \left(\frac{k_B T}{\Delta}\right)^4, \qquad (7)$$

given that $[\lambda(T)/\lambda(0) - 1] \propto (T/T_C)^2$ [49–51] for $T \leq 0.4\,T_C$. Confirming this hypothesis would require conducting magnetic-field measurements to assess the disorder of the films, as demonstrated in the work by Chockalingam *et al.* [52], which falls beyond the scope of our current study. Nevertheless, our experimental data exhibit remarkable agreement with this hypothesis, as illustrated by the yellow line in Fig. 6(c). The dirty-limit assumption is further justified by the discrepancy of the data with respect to BCS theory [53], implying

$$\frac{\Delta L_k}{L_k} = \frac{\lambda^2(T) - \lambda^2(0)}{\lambda^2(0)} \propto \sqrt{\frac{2\pi\,\Delta(0)}{T}} \exp\left(\frac{-\Delta}{T}\right). \quad (8)$$

As shown by the red line in Fig. 6(c), such an assumption does not reproduce the experimental data.

From the two fits of Eqs. (5) and (6) reported in Fig. 6, we extracted a thin-film critical temperature $T_C$ of 7.4 K, and TLS contribution $F\delta_{\mathrm{TLS}}^0$ of $1.8 \times 10^{-5}$, both in accordance with the previously obtained results reported in Figs. 2 and 5. We notice that for higher temperature the internal quality factor increases due to the saturation of TLS fluctuators, and then it starts dropping due to the losses caused by the quasiparticle population. Because of the large $T_C$ of the characterized film ($T_C \approx$ 7.5 K), this effect becomes dominant only at a temperature higher than 700 mK, i.e., at roughly 10% of $T_C$. The role played by TLS and quasiparticles is also confirmed by the temperature evolution of the resonator frequency

shift $\Delta f$ [see Fig. 6(c)]. Below 400 mK, $\Delta f$ is caused solely by TLS fluctuators, while at larger temperatures, the quasiparticle-induced shift dominates.

### D. Ageing characterization

Finally, to address the problem of thin films ageing, in particular the effect of the niobium oxide native layer on the internal quality factor [54–56], the devices were tested after nine months from the initial measurements, and in the same exact configuration. The devices were kept wire-bonded to the printed circuit boards and were stored in a pure $N_2$ atmosphere inside a Cleatech desiccator, with constant flow of $N_2$ of 30 sccm to ensure continuous purging. The temperature of the cabinet was kept between 21 and 23°C, with a relative humidity below 22%. We observed a systematic frequency shift dip of about $\Delta f_{\mathrm{age}}$ ranging between 3 and 5 MHz (see Table II) towards lower frequency for all the measured resonators. In Fig. 5 are collected the power scans of the internal quality factors of the tested resonators, with respect to average number of photons, measured right after fabrication (in blue) and after nine months (in red). While, for the low-$L_k$ devices, the quality factor dropped slightly due to ageing, for larger $L_k$ films, this effect is less pronounced, with the internal quality factor remaining almost unchanged after nine months. All the resonators remain, however, dominated by coupling to TLS, with internal quality factors at large number of photons in excess of $10^5$.

### V. DISCUSSION AND CONCLUSION

We have demonstrated high-internal-quality-factor ($Q_i > 10^5$), high-kinetic-inductance superconducting resonators operating in the single-photon regime based on
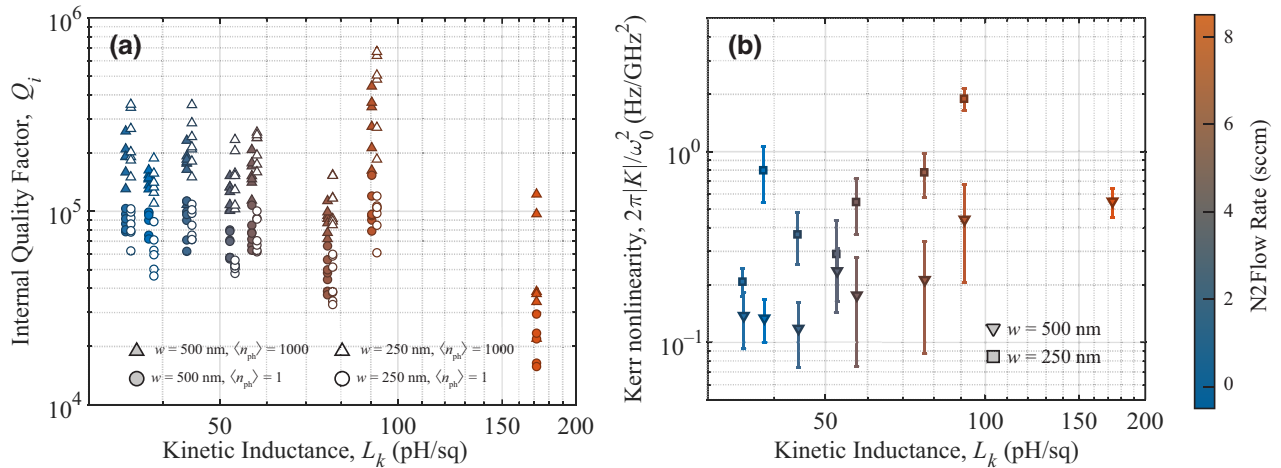


FIG. 7. (a) Internal quality factor of all the 105 tested resonators with respect to kinetic inductance $L_k$, resonator width, and photon number, as reported in the legend. The horizontal drift between the full and empty data points is an artifact to simplify graph reading. (b) Plot of self-Kerr nonlinearity $K$ normalized with respect to $\omega_0^2$ to highlight the qualitative linear dependence on kinetic inductance.

NbN thin-film superconductors. The NbN was bias sputtered to increase kinetic inductance and device yield due to its polycrystalline nature, at the expense of a reduced critical temperature.

Both stoichiometric and nonstoichiometric NbN films were deposited by varying the pressure conditions during deposition. After characterizing the deposition rates, films of equal thickness $\sim 13$ nm were sputtered. We fabricated and characterized 105 compact $LC$ resonators multiplexed in hanger configuration and with kinetic inductance ranging from 30 to 170 pH/$\Box$, as shown in Fig. 7(a). While for low photon number the internal quality factor presents a slight dependence on kinetic inductance, at high photon numbers the resonator quality factors exceed $5 \times 10^5$, suggesting a clear TLS-induced loss mechanism.

By fitting the high-power scattering parameter of the resonators, we also estimate the self-Kerr nonlinearity $K$ for the different tested films. Qualitatively, as depicted in Fig. 7(b), we notice a similar trend as in Ref. [25], suggesting a possible linear dependence of $K$ with respect to $L_k$, as expected from theory. The self-Kerr nonlinearity $K$, being below 100 Hz, is about four orders of magnitude lower than that of resonators made with Josephson junction arrays [57].

In conclusion, due to the increase of quality factor of at least a factor of 3 times for high power traces, the results show a clear dominance of TLS-induced losses across the board, with lower-kinetic-inductance films having larger internal quality factors, lower self-Kerr nonlinearity, and less robustness with respect to ageing effects. Overall, the study shows the possibility to trade off internal quality factor at low photon number with kinetic inductivity. This flexibility makes the technology particularly appealing for those applications relying on low nonlinearity and high quality factor at large average photon number, such as parametric amplifiers, readout resonators, and photon detectors.

## APPENDIX A: ESTIMATION OF KINETIC INDUCTANCE

The kinetic inductance of the films was estimated both using classical BCS theory and via Sonnet simulations, by simulating the resonant frequency of the tested chips and comparing it to the measured value at low photon number.

For the BCS theory estimation, the sheet resistance of the thin films $R_\Box$ was obtained by four-probe measurements at room temperature using a sheet resistance measurement system (CMT-SR2000N, Advanced Instrument Technology). We perform this measurement right after the deposition and before device processing (e.g., spin-coating, patterning, etching). For the critical temperature estimation, see Appendix B.
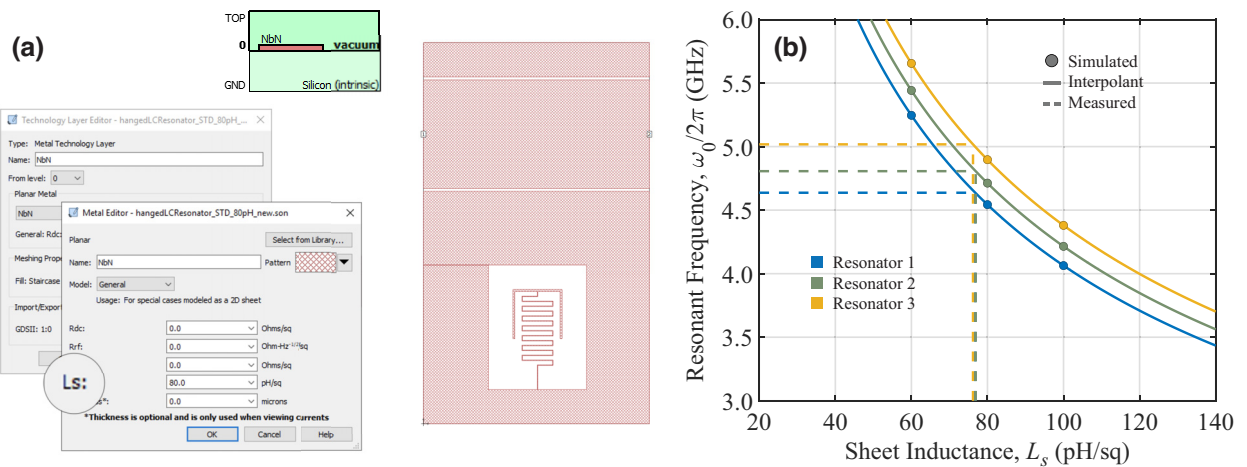


FIG. 8.　(a) Sonnet simulation setup. The NbN layer was modeled as a perfect conductor with variable sheet inductance $L_s$. (b) Interpolated kinetic inductivity versus resonant frequency curve for the three simulated resonators. Measuring the resonant frequency of each of the three simulated devices, it is possible to extract the kinetic inductivity of the superconducting film as the average of the three $L_s$ values.

For the kinetic inductance estimation using Sonnet, we used the measured resonant frequencies of the resonators. The chip designs were slightly different for the various films, to have the resonant frequencies of the devices in the same frequency range, and to ensure low reflections by matching as much as possible the microwave feedline to a 50-$\Omega$ impedance line. We used five designs overall.

For each design, we simulated three resonators with Sonnet to estimate their resonant frequency at three different sheet kinetic inductivity values $L_s$; see Fig. 8(a). Given that the resonator capacitance remains constant, the resonant frequency should follow a $\omega_0 \propto 1/\sqrt{L_k}$ dependence. By plotting the hyperbola passing through these three points, as shown in Fig. 8(b), it is possible, by measuring at low photon number the resonant frequency of the resonator under test $\omega_0/2\pi$, to estimate the kinetic inductance of the film. To increase the robustness of such a method, we average the obtained $L_k$ for the three resonators (see Fig. 8), allowing us to reduce even further the uncertainty associated with the kinetic inductivity of the films.

## APPENDIX B: CRITICAL TEMPERATURE ESTIMATION

The critical temperature was estimated by probing the microwave feedline of the devices in dc. The feedline was connected using filtered lines on each end (one BLP-23+ and one BLP-50+, MiniCircuits) and then probed using a source and measurement unit (SMU; Source Meter Unit 2604B, Keithley). The SMU measured the microwave feedline resistance by applying a current of 500 nA every 5 s and with a duty cycle of 4%. The reason for such a small current flow and pulsed measurement is multiple: On the one hand, the current should not warm up the device when in normal metal state, causing an offset in the measurement of $T_C$. On the other hand, the current should not be comparable to the critical current of the transmission line, causing a transition of the superconducting state due to the temperature-dependent depairing current relation. For all the microwave feedlines, we measured a critical current in the range of 1–5 mA at 800 mK, hence far enough from the used 500 nA.

For all the different films, the critical temperature $T_C$ is estimated as the temperature value at which the NbN film resistance is 50% of the resistance of the film at 10 K. The films' critical temperatures are collected both in Fig. 2 and in Table I. Figure 9 shows the different superconducting-metal transitions for different film compositions.

## APPENDIX C: DERIVATION OF EQUATIONS

The transmission spectra from the main feedline were measured at different input powers. The nonlinear effects of the kinetic inductance of the film produces an effective Kerr behavior of the resonators (see Fig. 3).

The nonlinear Kerr Hamiltonian for superconducting resonators can be written as [25]

$$H = \hbar\omega_0 a^\dagger a + \hbar\frac{K}{2}(a^\dagger a)^2, \tag{C1}$$

where $K \propto \Delta L \omega_0^2$ is the Kerr nonlinearity, $\Delta L$ is the inductance change, and $\omega_0$ is the fundamental resonator frequency. Following the same formalism as in Ref. [25,37] using input-output theory leads to the scattering parameter
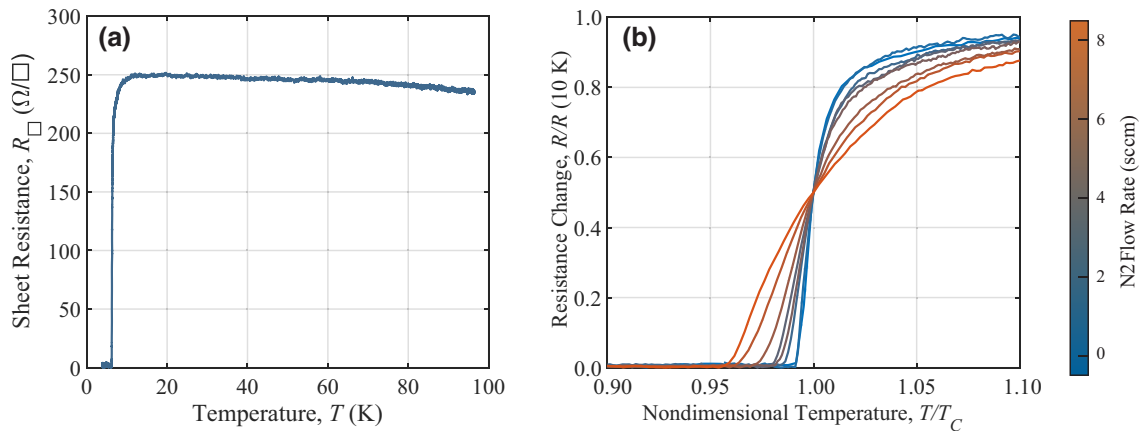


FIG. 9. (a) Sheet resistance versus temperature characteristic for a sample film. From the curve it is possible to estimate the residual resistivity ratio (RRR), defined as the ratio of the resistance of the film at low temperature before the superconducting transition and at room temperature, i.e., $R(10\ \text{K})/R(T_{\text{room}})$. The RRR values are reported in Table I for the different films. (b) Resistance versus temperature curve at the superconducting-metal transition for the various thin films. Increasing $N_2$ concentration causes the transition to broaden. The resistance change is nondimensionalized for all films with their value at $T = 10$ K, in accordance with the estimation of RRR

for hanger resonators of

$$S_{21} = 1 - \frac{\kappa}{\kappa + \gamma} \frac{e^{i\phi}}{\cos\phi} \frac{1}{1 + 2i(\delta - \xi n)}, \qquad (C2)$$

with

$$\delta \equiv \frac{\omega_d - \omega_0}{\kappa + \gamma}, \quad \xi \equiv \frac{|\tilde{\alpha}_{in}|^2 K}{\kappa + \gamma}, \quad n \equiv \frac{|\alpha|^2}{|\tilde{\alpha}_{in}|^2}. \qquad (C3)$$

In the above, $\tilde{\alpha}_{in} \equiv \sqrt{\kappa}\alpha_{in}/(\kappa + \gamma)$; $\kappa \equiv \omega_0/Q_c$ is the coupling to the feedline; $\gamma \equiv \omega_0/Q_i$ is the internal resonator loss; $\phi$ is a parameter used to take into account impedance mismatch between the feedline and the resonator, also called the $\phi$ rotation method ($\phi$RM) [43]; and $n$ is calculated as the solution of the equation

$$\frac{1}{2} = \left(\delta^2 + \frac{1}{4}\right)n - 2\delta\xi n^2 + \xi^2 n^3. \qquad (C4)$$

Cryogenic attenuated input lines were calibrated at base temperature and an extra contribution of $-8$ dB was estimated from the coaxial lines, for a total attenuation of $-68$ dB. Nonlinear effects described herein have been analyzed from the assumption that the input power is known within an error of $\pm 2$ dB. The average photon number $\langle n_{\mathrm{ph}} \rangle = |\tilde{\alpha}_{in}|^2$ in the resonator,

$$|\tilde{\alpha}_{in}|^2 = \frac{\kappa}{(\kappa + \gamma)^2} \frac{P_{\mathrm{in}}}{\hbar\omega_0}, \qquad (C5)$$

together with Eq. (C5), allows one to estimate the Kerr nonlinearity $K$ from the fitting function parameters $\xi$ and $n$:

$$K = \xi \frac{(\kappa + \gamma)}{|\tilde{\alpha}_{in}|^2}. \qquad (C6)$$

Using the generalized relation of current dependence of kinetic inductance derived in Ref. [58], in the limit for small $I/I_c$, we obtain

$$L_k = L_{k,0}(1 - (I/I_c)^{n_{\mathrm{fr}}})^{-1/n_{\mathrm{fr}}}$$
$$\approx L_{k,0}\left(1 + \frac{1}{n_{\mathrm{fr}}}\left(\frac{I}{I_c}\right)^{n_{\mathrm{fr}}}\right). \qquad (C7)$$

Substituting Eq. (C7) in the relation for the Kerr nonlinearity gives

$$K \propto \Delta L \omega_0^2 \propto \frac{L_{k,0}\omega_0^2}{I_c^{n_{\mathrm{fr}}}}, \qquad (C8)$$

where $L_{k,0}$ is the kinetic inductance of the superconducting film at zero bias current, $n_{\mathrm{fr}} = 2.21$ is the exponential of the fast relaxation limit function defined in Ref. [58], and

$I$ is the bias current, which is proportional to the pump power $P_{\mathrm{in}}$. In order to compare the nonlinearity of the tested devices, we have measured the critical current of the coupling feedline so to have an estimate of the critical current $I_c$.

[1] M. Kjaergaard, M. E. Schwartz, J. Braumüller, P. Krantz, J. I.-J. Wang, S. Gustavsson, and W. D. Oliver, Superconducting qubits: Current state of play, Annu. Rev. Condens. Matter Phys. **11**, 369 (2020).

[2] M. Scigliuzzo, G. Calajò, F. Ciccarello, D. Perez Lozano, A. Bengtsson, P. Scarlino, A. Wallraff, D. Chang, P. Delsing, and S. Gasparinetti, Controlling Atom-Photon Bound States in an Array of Josephson-Junction Resonators, Phys. Rev. X **12**, 031036 (2022).

[3] V. E. Manucharyan, J. Koch, L. I. Glazman, and M. H. Devoret, Fluxonium: Single Cooper-pair circuit free of charge offsets, Science **326**, 113 (2009).

[4] R. Kuzmin, R. Mencia, N. Grabon, N. Mehta, Y.-H. Lin, and V. E. Manucharyan, Quantum electrodynamics of a superconductor–insulator phase transition, Nat. Phys. **15**, 930 (2019).

[5] N. A. Masluk, I. M. Pop, A. Kamal, Z. K. Minev, and M. H. Devoret, Microwave Characterization of Josephson Junction Arrays: Implementing a Low Loss Superinductance, Phys. Rev. Lett. **109**, 137002 (2012).

[6] A. Stockklauser, P. Scarlino, J. V. Koski, S. Gasparinetti, C. K. Andersen, C. Reichl, W. Wegscheider, T. Ihn, K. Ensslin, and A. Wallraff, Strong Coupling Cavity QED with Gate-Defined Double Quantum Dots Enabled by a High Impedance Resonator, Phys. Rev. X **7**, 011030 (2017).

[7] A. J. Annunziata, D. F. Santavicca, L. Frunzio, G. Catelani, M. J. Rooks, A. Frydman, and D. E. Prober, Tunable superconducting nanoinductors, Nanotechnology **21**, 445202 (2010). http://stacks.iop.org/0957-4484/21/i=44/a=445202

[8] N. Maleeva, L. Grünhaupt, T. Klein, F. Levy-Bertrand, O. Dupre, M. Calvo, F. Valenti, P. Winkel, F. Friedrich, W. Wernsdorfer, A. V. Ustinov, H. Rotzinger, A. Monfardini, M. V. Fistul, and I. M. Pop, Circuit quantum electrodynamics of granular aluminum resonators, Nat. Commun. **9**, 3889 (2018).

[9] S. Kono, K. Koshino, D. Lachance-Quirion, A. F. van Loo, Y. Tabuchi, A. Noguchi, and Y. Nakamura, Breaking the trade-off between fast control and long lifetime of a superconducting qubit, Nat. Commun. **11**, 3683 (2020).

[10] C. Wang, et al., Towards practical quantum computers: Transmon qubit with a lifetime approaching 0.5 milliseconds, Npj Quantum Inf. **8**, 3 (2022).

[11] T. C. White, et al., Traveling wave parametric amplifier with Josephson junctions using minimal resonator phase matching, Appl. Phys. Lett. **106**, 242601 (2015).

[12] C. Macklin, K. O. Brien, D. Hover, M. E. Schwartz, V. Bolkhovsky, X. Zhang, W. D. Oliver, and I. Siddiqi, A near quantum-limited Josephson traveling-wave parametric amplifier, Science **350**, 307 (2015).

[13] P. Winkel, K. Borisov, L. Grünhaupt, D. Rieger, M. Spiecker, F. Valenti, A. V. Ustinov, W. Wernsdorfer, and I. M. Pop, Implementation of a Transmon Qubit Using

Superconducting Granular Aluminum, Phys. Rev. X **10,** 031032 (2020).

[14] P. Day, H. Leduc, B. A Mazin, A. Vayonakis, and J. Zmuidzinas, A broadband superconducting detector suitable for use in large arrays, Nature **425,** 817 (2003).

[15] B. Ho Eom, P. K. Day, H. G. LeDuc, and J. Zmuidzinas, A wideband low-noise superconducting amplifier with high dynamic range, Nat. Phys. **8,** 623 (2012).

[16] G. N. Gol´tsman, O. Okunev, G. Chulkova, A. Lipatov, A. Semenov, K. Smirnov, B. Voronov, A. Dzardanov, C. Williams, and R. Sobolewski, Picosecond superconducting single-photon optical detector, Appl. Phys. Lett. **79,** 705 (2001).

[17] B. Cabrera, R. M. Clarke, P. Colling, A. J. Miller, S. Nam, and R. W. Romani, Detection of single infrared, optical, and ultraviolet photons using superconducting transition edge sensors, Appl. Phys. Lett. **73,** 735 (1998).

[18] D. J. Parker, M. Savytskyi, W. Vine, A. Laucht, T. Duty, A. Morello, A. L. Grimsmo, and J. J. Pla, Degenerate parametric amplification via three-wave mixing using kinetic inductance, Phys. Rev. Appl. **17,** 034064 (2022).

[19] M. R. Vissers, J. Hubmayr, M. Sandberg, S. Chaudhuri, C. Bockstiegel, and J. Gao, Frequency-tunable superconducting resonators via nonlinear kinetic inductance, Appl. Phys. Lett. **107,** 062601 (2015).

[20] A. A. Adamyan, S. E. Kubatkin, and A. V. Danilov, Tunable superconducting microstrip resonators, Appl. Phys. Lett. **108,** 172601 (2016).

[21] M. H. Devoret, S. Girvin, and R. Schoelkopf, Circuit-QED: How strong can the coupling between a Josephson junction atom and a transmission line resonator be?, Ann. Phys. **16,** 767 (2007).

[22] A. F. Kockum, A. Miranowicz, S. D. Liberato, S. Savasta, and F. Nori, Ultrastrong coupling between light and matter, Nat. Rev. Phys. **1,** 19 (2019).

[23] P. Forn-Díaz, L. Lamata, E. Rico, J. Kono, and E. Solano, Ultrastrong coupling regimes of light-matter interaction, Rev. Mod. Phys. **91,** 025005 (2019).

[24] D. Niepce, J. Burnett, and J. Bylander, High kinetic inductance NbN nanowire superinductors, Phys. Rev. Appl. **11,** 044014 (2019).

[25] A. Anferov, A. Suleymanzade, A. Oriani, J. Simon, and D. I. Schuster, Millimeter-wave four-wave mixing via kinetic inductance for quantum devices, Phys. Rev. Appl. **13,** 024056 (2020).

[26] N. Samkharadze, A. Bruno, P. Scarlino, G. Zheng, D. P. DiVincenzo, L. DiCarlo, and L. M. K. Vandersypen, High-kinetic-inductance superconducting nanowire resonators for circuit QED in a magnetic field, Phys. Rev. Appl. **5,** 044004 (2016).

[27] H. G. Leduc, B. Bumble, P. K. Day, B. H. Eom, J. Gao, S. Golwala, B. A. Mazin, S. McHugh, A. Merrill, D. C. Moore, O. Noroozian, A. D. Turner, and J. Zmuidzinas, Titanium nitride films for ultrasensitive microresonator detectors, Appl. Phys. Lett. **97,** 102509 (2010).

[28] L. Grünhaupt, M. Spiecker, D. Gusenkova, N. Maleeva, T. Skacel, I. Takmakov, F. Valenti, P. Winkel, H. Rotzinger, W. Wernsdorfer, A. V. Ustinov, and I. M. Pop, Granular aluminium as a superconducting material for high-impedance quantum circuits, Nat. Mater. **18,** 816 (2019). https://www.nature.com/articles/s41563-019-0350-3

[29] M. R. Vissers, J. Gao, D. S. Wisbey, D. A. Hite, C. C. Tsuei, A. D. Corcoles, M. Steffen, and D. P. Pappas, Low loss superconducting titanium nitride coplanar waveguide resonators, Appl. Phys. Lett. **97,** 232509 (2010).

[30] P. Krantz, M. Kjaergaard, F. Yan, T. P. Orlando, S. Gustavsson, and W. D. Oliver, A quantum engineer's guide to superconducting qubits, Appl. Phys. Rev. **6,** 021318 (2019).

[31] M. Shaw, F. Marsili, A. Beyer, R. Briggs, J. Allmaras, and W. H. Farr, in *Free-Space Laser Communication and Atmospheric Propagation XXIX*, Vol. 10096, edited by H. Hemmati and D. M. Boroson, International Society for Optics and Photonics (SPIE, 2017) p. 145.

[32] H. Takesue, S. W. Nam, Q. Zhang, R. H. Hadfield, T. Honjo, K. Tamaki, and Y. Yamamoto, Quantum key distribution over a 40-dB channel loss using superconducting single-photon detectors, Nat. Photonics **1,** 343 (2007).

[33] F. Bussiéres, C. Clausen, A. Tiranov, B. Korzh, V. B. Verma, S. W. Nam, F. Marsili, A. Ferrier, P. Goldner, H. Herrmann, C. Silberhorn, W. Sohler, M. Afzelius, and N. Gisin, Quantum teleportation from a telecom-wavelength photon to a solid-state quantum memory, Nat. Photonics **8,** 775 (2014).

[34] M. Scigliuzzo, L. E. Bruhat, A. Bengtsson, J. J. Burnett, A. F. Roudsari, and P. Delsing, Phononic loss in superconducting resonators on piezoelectric substrates, New. J. Phys. **22,** 053027 (2020).

[35] A. E. Dane, A. N. McCaughan, D. Zhu, Q. Zhao, C.-S. Kim, N. Calandri, A. Agarwal, F. Bellei, and K. K. Berggren, Bias sputtered NbN and superconducting nanowire devices, Appl. Phys. Lett. **111,** 122601 (2017).

[36] C. R. H. McRae, H. Wang, J. Gao, M. R. Vissers, T. Brecht, A. Dunsworth, D. P. Pappas, and J. Mutus, Materials loss measurements using superconducting microwave resonators, Rev. Sci. Instrum. **91,** 091101 (2020).

[37] C. Eichler and A. Wallraff, Controlling the dynamic range of a Josephson parametric amplifier, EPJ Quantum Technol. **1,** 2 (2014).

[38] S. Probst, F. B. Song, P. A. Bushev, A. V. Ustinov, and M. Weides, Efficient and robust analysis of complex scattering data under noise in microwave resonators, Rev. Sci. Instrum. **86,** 024706 (2015).

[39] M. V. Burdastyh, S. V. Postolova, T. Proslier, S. S. Ustavshikov, A. V. Antonov, V. M. Vinokur, and A. Y. Mironov, Superconducting phase transitions in disordered NbTiN films, Sci. Rep. **10,** 1471 (2020).

[40] C. Müller, J. H. Cole, and J. Lisenfeld, Towards understanding two-level systems in amorphous solids: Insights from quantum circuits, Rep. Prog. Phys. **82,** 124501 (2019).

[41] W. A. Phillips, Tunneling states in amorphous solids, J. Low Temp. Phys. **7,** 351 (1972).

[42] P. W. Anderson, B. I. Halperin, and C. M. Varma, Anomalous low-temperature thermal properties of glasses and spin glasses, Philos. Mag.: J. Theor. Exp. Appl. Phys. **25,** 1 (1972).

[43] J. Gao, Ph.D. thesis, 2008, https://thesis.library.caltech.edu/2530/.

[44] D. P. Pappas, M. R. Vissers, D. S. Wisbey, J. S. Kline, and J. Gao, Two level system loss in superconducting microwave resonators, IEEE Trans. Appl. Supercond. **21,** 871 (2011).

[45] G. J. Grabovskij, T. Peichl, J. Lisenfeld, G. Weiss, and A. V. Ustinov, Strain tuning of individual atomic tunneling

systems detected by a superconducting qubit, Science **338,** 232 (2012).

[46] A. Bilmes, S. Volosheniuk, J. D. Brehm, A. V. Ustinov, and J. Lisenfeld, Quantum sensors for microscopic tunneling systems, Npj Quantum Inf. 7, 27 (2021).

[47] R. Barends, J. Wenner, M. Lenander, Y. Chen, R. C. Bialczak, J. Kelly, E. Lucero, P. O'Malley, M. Mariantoni, D. Sank, H. Wang, T. C. White, Y. Yin, J. Zhao, A. N. Cleland, J. M. Martinis, and J. J. A. Baselmans, Minimizing quasiparticle generation from stray infrared light in superconducting quantum circuits, Appl. Phys. Lett. **99,** 113507 (2011).

[48] C. X. Yu, S. Zihlmann, G. Troncoso Fernández-Bada, J.-L. Thomassin, F. Gustavo, É. Dumur, and R. Maurand, Magnetic field resilient high kinetic inductance superconducting niobium nitride coplanar waveguide resonators, Appl. Phys. Lett. **118,** 054001 (2021).

[49] G. M. Eliashberg, G. V. Klimovitch, and A. V. Rylyakov, On the temperature dependence of the London penetration depth in a superconductor, J. Supercond. **4,** 393 (1991).

[50] A. Shoji, S. Kiryu, and S. Kohjiro, Superconducting properties and normal-state resistivity of single-crystal NbN films prepared by a reactive rf-magnetron sputtering method, Appl. Phys. Lett. **60,** 1624 (1992).

[51] J. Lee and T. R. Lemberger, Penetration depth $\lambda(T)$ of $YBa_2Cu_3O_{7-\delta}$ films determined from the kinetic inductance, Appl. Phys. Lett. **62,** 2419 (1993).

[52] S. P. Chockalingam, M. Chand, J. Jesudasan, V. Tripathi, and P. Raychaudhuri, Superconducting properties and Hall effect of epitaxial NbN thin films, Phys. Rev. B **77,** 214503 (2008).

[53] R. Prozorov and V. G. Kogan, London penetration depth in iron-based superconductors, Rep. Prog. Phys. **74,** 124505 (2011).

[54] D. F. Santavicca and D. E. Prober, Aging of ultra-thin niobium films, IEEE Trans. Appl. Supercond. **25,** 1 (2015).

[55] O. Medeiros, M. Colangelo, I. Charaev, and K. K. Berggren, Measuring thickness in thin NbN films for superconducting devices, J. Vac. Sci. Technol. A **37,** 041501 (2019).

[56] J. Verjauw, A. Potočnik, M. Mongillo, R. Acharya, F. Mohiyaddin, G. Simion, A. Pacco, T. Ivanov, D. Wan, A. Vanleenhove, L. Souriau, J. Jussot, A. Thiam, J. Swerts, X. Piao, S. Couet, M. Heyns, B. Govoreanu, and I. Radu, Investigation of microwave loss induced by oxide regrowth in high-$Q$ niobium resonators, Phys. Rev. Appl. **16,** 014018 (2021).

[57] Y. Krupko, V. D. Nguyen, T. Weißl, E. Dumur, J. Puertas, R. Dassonneville, C. Naud, F. W. J. Hekking, D. M. Basko, O. Buisson, N. Roch, and W. Hasch-Guichard, Kerr nonlinearity in a superconducting Josephson metamaterial, Phys. Rev. B **98,** 094516 (2018).

[58] J. R. Clem and V. G. Kogan, Kinetic impedance and depairing in thin and narrow superconducting films, Phys. Rev. B **86,** 174521 (2012).